

1 **An Early Triassic (Smithian) stromatolite associated with giant ooid**
2 **banks from Lichuan (Hubei Province), South China: environment and**
3 **controls on its formation**

4 Yuheng Fang^a, Zhong-Qiang Chen^a *, Stephen Kershaw^b, Mao Luo^{a,c}

5 ^a State Key Laboratory of Biogeology and Environmental Geology, China University of
6 Geosciences (Wuhan), Wuhan 430074, China

7 ^b Institute for Environment, Brunel University, Uxbridge, UB8 3PH, UK

8 ^c School of Life and Environmental Sciences, Deakin University, Melbourne Burwood
9 Campus, 221 Burwood Highway, Burwood, VIC 3125, Australia.

10 * Corresponding author: zhong.qiang.chen@cug.edu.cn

11
12 **Abstract**

13 As a consequence of the Permian–Triassic mass extinction (PTME), the
14 microbe-dominated ecosystems proliferated in shallow marine settings worldwide, and
15 they are indicated by the widespread ‘anachronistic facies’ in the Lower Triassic
16 successions. Of these, both microbialite and giant ooid are most widely distributed, and
17 these unusual biosedimentary structures not only are commonly present in the
18 Permian–Triassic boundary beds, but also extend through the entire Lower Triassic
19 successions. Here, we report a probably the known thickest Early Triassic stromatolite,
20 which developed within giant ooid banks from the late Smithian succession (Lower
21 Triassic) of the Lichuan area, western Hubei Province, South China. Therein a ~18 m
22 thick stromatolite is embedded within ~30 m thick oolitic limestones that crop out at the
23 upper Daye Formation. The associated conodonts suggest a late Smithian (Early Triassic)
24 age for the stromatolite-ooid complex. These pronounced ooids can be categorized into
25 circular, compound, superficial, and irregular ooids. Stromatolites exhibit domical,
26 stratified columnar, wavy laminated, cabbage-shaped, roll-up, and conical structures.
27 Stromatolites are overlain by thick oolitic limestone, implying that the demise of the
28 Lichuan stromatolite may be attributed to destruction by agitated shallow waters. Four
29 types of microbially induced microstructures are recognizable in stromatolites. The layers
30 with intense fluorescence indicative of microbial organomineralization contribute to the
31 formation of the ooids. Moreover, the common occurrence of nanometer-scale textures
32 relative to the formation of the dolomite both in stromatolite and ooids, as well as
33 authigenic quartz grains commonly preserving in stromatolite, could be attributed to
34 abundant organic matters in water, resulting from microbial proliferations. As such,
35 microbes were probably extremely flourishing in both eastern and western margins of the
36 Palaeo-Tethys Ocean during middle Early Triassic, suggesting the long-term degradation
37 of marine ecosystems after the PTME.

38
39 *Keywords:* stromatolites; giant ooid; microbial origin; ecosystem degradation; Early
40 Triassic; Lichuan; South China

41
42 **1. Introduction**

43
44 The aftermath of the Permian–Triassic mass extinction (PTME) was a tough time for
45 the inhabitation of metazoans but witnessed the widespread proliferation of
46 microbe-dominated communities in marine and terrestrial ecosystems (Pruss and Bottjer,

47 1999; Lehrmann, 1999; Kershaw et al., 1999, 2001, 2007, 2011, 2012; Ezaki et al., 2003,
48 2008, 2012; Wang et al., 2005; Pruss et al., 2006; Baud et al., 2007; Mary and Woods,
49 2008; Chen and Benton, 2012; Chen et al., 2014; Lehrmann et al., 2015; Chu et al., 2015;
50 Tu et al., 2016; Luo et al., 2016; Xu et al., 2016; Fang et al., 2016). Such a phenomenon
51 of metazoan depletion coupled with microbial proliferation could be triggered by
52 recurrent environmental shocks such as global warming, oceanic acidification, and
53 widespread anoxia that may also have prevailed in the PTME but repeated over the next 5
54 Myr until latest Olenekian (Chen and Benton, 2012). Thus, unusual biosedimentary
55 structures indicate the Earth's ecosystems have changed fundamentally after the greatest
56 biocrisis of Earth history (Erwin, 2006; Chen and Benton, 2012). To date, six peak
57 temporal pulses of microbialite occurrence have been recognized from the immediate
58 aftermath of the PTME to the biotic full recovery period in middle-late Anisian (Chen
59 and Benton, 2012), corresponding to the early Griesbachian, late Griesbachian to early
60 Dienerian, early Smithian, late Smithian, late Spathian, and early Anisian, respectively
61 (Pruss et al., 2006; Baud et al., 2007; Kershaw et al., 2012; Chen et al., 2014; Luo et al.,
62 2014). Unlike metazoan reef buildups, these post-extinction microbial reef deposits
63 possess relatively low geometry, often 1-5 m in thickness. Here, we report an 18 m-thick
64 stromatolite deposit that grew on a thick giant ooid bank from the Lower Triassic Daye
65 Formation of the Lichuan area, western Hubei Province, South China (Fig. 1). The newly
66 found stromatolite-oolite complex is >30 m in thickness and is preserved in the upper
67 part of the fourth member of the Daye Formation (Fig. 2). Apart from the exceptionally
68 thick stromatolite, giant ooids from the Lichuan buildup are also pronounced in the field
69 (Mei et al., 2008). Recently, these giant ooids have also been considered as the
70 precipitation products of microbe activities in saturated seawater in carbonate settings
71 and commonly occurred in the aftermath of major mass extinctions (Li et al., 2013, 2015).
72 Geobiological features of both stromatolites and giant ooid bank therefore provide
73 insights into the seawater conditions in the aftermath of the LPME in carbonate
74 platforms.

75 This paper aims to document geobiologic features of an early Triassic
76 stromatolite-giant ooid complex from Lichuan City, Hubei Province, South China (Fig. 1)
77 and attempts to test its biogenesis. Geobiologic process of key nanometer-scale structures
78 in dolomite and authigenic quartz grains embedded in stromatolite and/or oolite is also
79 emphasized based on detailed micro-analysis. The possible constructors of stromatolite
80 and their growing environments are also discussed in a broad context by comparing the
81 Lichuan example with other post-extinction microbialites from around the world.

82

83 **2. Geological setting and stratigraphy**

84

85 The Lichuan stromatolite-oolite bank complex is exposed at the Daxiandong quarry,
86 ~12 km northwest of Lichuan City, western Hubei Province, South China (Fig. 1). The
87 Lichuan area was located at the northwestern margin of the upper Yangtze Platform,
88 which was a huge inheriting carbonate platform lying on the middle of the South China
89 Block during the Permian–Triassic (P–Tr) transition (Feng et al., 1997). Therein the Daye
90 Formation is dominated by shallow platform facies carbonates and is subdivided into four
91 members: black shale (Member 1), dark grey limestone (Member 2), reddish micrites
92 (Member 3), and oolite-dominated micrite limestone (Member 4) (Wang et al., 1981).

93 Of these, Member 4 is well exposed at the Daxiandong quarry, and comprises five
94 beds: ~1 m-thick oolite resting on light reddish micritic limestone (Bed 1), massive
95 stromatolite (>14 m in thickness) (Bed 2), 1 m-thick oolite (Bed 3), ~2 m-thick
96 stromatolite with thin rotelliform oolite layers (Bed 4), and 12 m-thick oolite (Bed 5),
97 which is also the top of the Daye Formation (Fig. 3B). Thus, three oolite units
98 interbedded with two stromatolite layers characterize the upper Daye Formation. Oolite
99 units thicken, with enlarging ooids up the section. The stromatolite-oolite complex is
100 capped by the medium-bedded laminated muddy limestone of the Jialingjiang Formation
101 (Fig. 3A).

102 Except for the stromatolites, the oolite shoaling and bank facies characterize the
103 Daye Formation successions in the Yangtze Platform of the eastern Sichuan Basin. Wu et
104 al. (1994) recognized four development stages of ooid shoals and banks during the Early
105 Triassic (Fig. 2). Controlled by transgression-regression progress in the Induan to
106 Olenekian age of the Early Triassic, the stromatolite-oolite complex has undergone the
107 obvious progradation from the west to the east. Thus, resulting from this sedimentary
108 process, these stromatolite-oolite complex have the thickness of >30 meters, which
109 developed in the upper part of the Daye Formation.

110 Wang et al. (1981) established conodonts *Neospathodus dieneri*, *Neospathodus*
111 *pakistanensis*, and *Neospathodus waageni* Zones from the middle and upper parts of the
112 Daye Formation in the neighboring Daxiandong section of Lichuan area. The first zone is
113 characteristic of the Dienerian fauna, while the latter two are usually assigned to early
114 Smithian in age in South China (Zhao et al., 2007, 2013). The Lichuan stromatolite-oolite
115 complex is embedded between the *N. pakistanensis* and *N. waageni* Zones, and thus is
116 early Smithian in age (Fig. 3B).

117 118 **3. Materials and methods**

119
120 Polished slabs of stromatolite were made for observing micro-structures. Petrologic
121 thin sections of both stromatolites and oolites were made to examine fabrics and
122 diagenetic features. In order to observe possible microbial signatures within stromatolites
123 and oolites, some freshly broken and polished chips of laminated structure within
124 stromatolites and ooids were prepared for Scanning Electron Microscope (SEM) imaging
125 analysis. These samples were cleaned first by diluted water and then etched with 0.5 %
126 chloride acid for 3–5 s, followed by a second rinse by diluted water and ethyl alcohol.
127 Some samples for SEM analysis were polished with 200 mesh diamond dust before
128 chemical etching and cleaning. Samples were all coated with platinum for surface texture
129 analysis and energy dispersive X-ray spectrometry (EDS) analysis. Surface texture
130 micro-analysis was initially conducted using the Field Emission Scanning Electron
131 Microscope Hitachi SU8010 equipped at the State Key Laboratory of Biogeology and
132 Environmental Geology, China University of Geosciences (Wuhan), China. Fluorescent
133 imaging analysis is undertaken to check for the distribution of residual organic matter in
134 stromatolite using a fluorescent microscopy equipped at the China University of
135 Geosciences (Wuhan), China. Terminology and methods describing stromatolite features
136 follow Shapiro (2000), who observed and classified microbial fabrics at macro-, meso-,
137 and micro-structural scales.

139 **4. Results**

140
141 *4.1 Macro- and meso-structures of stromatolite*

142
143 On the outcrop, domical or columnar stromatolites are densely compacted laterally
144 and closely piled up longitudinally (Fig. 4A–C). Stromatolites from outcrop exhibit a
145 wide variety of macrostructures: domical, stratified columnar, wavy laminated,
146 cabbage-shaped, roll-up, and conical structures (Figs 4–5), which are displayed on a large
147 limestone wall at the quarry (Fig. 4A). Of these, the cabbage-like forms, 20–50 cm wide
148 and 20–40 cm high, are rather pronounced on the wall (Figs 4B–C, 5B). Columnar
149 stromatolites are ~20 cm wide and 30 cm high (Fig. 4E), and its tops were eroded by
150 agitated waves and surrounded by ooids occasionally (Fig. 4E). Some columns branch
151 upwards (Fig. 4D). The wavy laminated stromatolites contain crinkled thin layers with
152 each layer being ~1 cm thick and extending laterally (Fig. 5A). In some cases, the
153 crinkled thin layers of stromatolites form roll-up structures (Fig. 5C–D), which indicate
154 soft microbial layers stirred by strong waves. Domical stromatolites are >20 cm high and
155 30 cm wide (Fig. 5E). Conical stromatolites are ~10 cm wide and >20 cm high (Fig. 5F).
156 Some single stromatolites show multiple macrostructures at the same time. They all,
157 however, have alternations of laminae. The alternating dark-colored thin laminae and
158 light-colored laminae are conspicuous on polished blocks (Fig. 5B–E).

159
160 *4.2 Micro- to ultra-structures of stromatolites*

161
162 Under polarizing microscope, stromatolites are characterized by undulating
163 laminations embedding with rare skeletal grains (Fig. 6A). The diffuse laminated,
164 reticular, intraclastic, and irregular clotted microstructures are recognized from the
165 Lichuan stromatolites, and they are described as below.

166
167 *4.2.1 Diffuse laminated microstructures (DLMs)*

168
169 The DLM is dominated by poorly-defined laminae in variable thicknesses (Fig. 6A).
170 Dark colored laminae consist of concentrations of organic inclusions that extend laterally
171 for millimeters to centimeters. They are separated by light colored zones of
172 microcrystalline carbonate with few inclusions. The contact between dark and light
173 colored laminae is marked by a gradual variation in color, reflecting variable
174 concentrations of organic inclusions and crystal sizes.

175 Laminae are different in thickness and embrace varied geometry of couplets of dark
176 laminae and interstitial microcrystalline carbonate. Abundant laminated microstructures
177 consist of dark laminae that vary between 30 and 50 microns in thickness. Some dark
178 colored laminae are much thicker, 100–300 microns in thickness (Fig. 6A). Both thin and
179 thick laminae appear as planar geometries in thin section and, occasionally, as slightly
180 domal, or contorted, or rolled up in shapes. Some crinkled laminations form the reticular
181 microstructures (Fig. 6B–C; see below).

182
183 *4.2.2 Reticular microstructures (RMs)*

184

185 The RM is typically preserved in stromatolite (Figs 6B–C, 7A–B). They are
186 comprised of light-colored, coarse calcite and dark-colored micrite as well as opacity
187 materials (Figs 6B–C, 7A–B). RMs form thin micritic laminae in low power lens (Fig.
188 6A). Reticulations are loosely combined and form clotted textures in some parts, similar
189 to thrombolite textures (Figs 6B, 7A). Fabrics that construct the dark-colored reticular
190 frameworks are 20–100 μm thick and composed of concentrations of nodes that usually
191 extend laterally (Fig. 6C). Fabrics are occasionally arc-shaped or semi-circular, and
192 construct chamber-like structures (Fig. 7B).

193 194 *4.2.3 Intraclastic microstructure (IM)*

196 The IM is characterized by brown colored, isolated intraclasts (Fig. 7C–D), which
197 are irregular, usually larger than 300 μm in size, and made up of coarse dolomite grains.
198 Dark colored micrite envelope coating intraclasts is distinct, and may have resulted from
199 decompositions of microbial mat that wrapped up intraclasts before lithification and
200 diagenesis (Fig. 7C–D). Matrix is divided by clumps and shows vein-shaped
201 microstructure. Vein-shaped microstructure is 100–200 μm wide and partially similar to
202 bird-foot structure. SEM imaging clearly exhibits that intraclasts are made up of
203 subhedral to euhedral dolomites, and possess high magnesium contents (Fig. 8A–C).

204 205 *4.2.4 Irregular clotted microstructure (ICM)*

206
207 The ICM consists of diffuse to distinct irregularly shaped patches or rounds of dark
208 microcrystalline carbonates. These clots vary in size, shape, and spacing (Fig. 7E–F).
209 They are typically elongate and irregularly shaped, and are occasionally associated with
210 ooids, indicating active disturbance of currents (Fig. 7E). Clots possess diameter ranging
211 from <100 μm to 500 μm and are surrounded by light colored microcrystalline carbonate.
212 The alignment of dispersed clots commonly defines a diffuse lamination (Fig. 7E). Some
213 clots under high-magnification microscope also show that smaller dark rounded microclot
214 individuals are visible at their outer margins (Fig. 7F). In contrast to diffuse laminated
215 microstructures, ICMs do not occur within mesoclots.

216 217 *4.2.5 Ultra-structures of stromatolites*

218
219 Under the SEM, quartz crystals are commonly present in stromatolite
220 microstructures. They coexist with minute dolomite rhombs within stromatolitic laminae.
221 Quartz crystals are usually euhedral in outline (Fig. 8D), showing no signs of abrasion.
222 They scatter in stromatolite laminae and do not concentrate to form layers or horizons,
223 which are typical of detrital quartz grains. These crystals therefore are likely authigenic in
224 origin, showing no sign of transportation (Fig. 8D). Dolomite in stromatolite laminae has
225 distinct nanometer-scale structure in its surfaces (Fig. 8E–F). These tiny objects are
226 mostly amorphous. Some nano-particles are lumpy-shaped, and have diameter ranging
227 from 100 nm to 200 nm (Fig. 8E–F).

228 229 *4.3 Macro- and meso-structures of ooids*

230

231 Ooids are a common component of shallow facies of the Upper Daye Formation and
232 are readily observed on outcrop (Fig. 9). They are typically present in packstone and
233 grainstone, and appear massive ooid aggregates (Fig. 9B–C). Some ooids also
234 concentrate in some thin layers, 0.3–1.5 cm in thickness, to form ‘ooid laminations’ (Fig.
235 9A). Individual ooids are spherical, ellipsoidal or even irregularly rounded in shapes, and
236 are typically 0.2–2 mm in diameter, although few ooids are >2 mm in diameter (Fig.
237 9B–C).

238

239 *4.4 Micro- to ultra-structures of ooids*

240

241 The Lichuan ooids can be categorized into four types: circular, compound,
242 superficial (thin), and irregular ooids (Fig. 10). Circular ooids are spherical to ellipsoidal
243 in outline, and are usually poorly sorted, well-rounded, typically 0.2–2 mm in diameter.
244 They comprise micrite peloidal or sparitic nuclei surrounded by concentrically laminated
245 to homogenous micrite coating layers (Fig. 10B–C). Individual lamina within
246 concentrically-laminated ooids ranges from 10 to 30 μm in thickness. The laminae
247 consist of alternating layers of equal or nearly equal thickness of dark coloured micrite
248 and light coloured micrite that embeds occasionally euhedral dolomite crystals (Fig.
249 10B–D). Compound forms are composed of multiple previously cemented ooids (Fig.
250 10E–F). Superficial ooids have very thin cortical coating and specifically ooid in which
251 the thickness of the accretionary coating is less, or commonly far less than the radius of
252 the nucleus (see smaller ooids in Fig. 10A). The last type of ooids includes irregularly
253 shaped or broken, regrowth grains (Fig. 10D). In some samples, ooid layers alternate with
254 relatively dark coloured stromatolite layers (Fig. 11). Dark coloured layers between two
255 ooid layers are characterized by their cross-bedding feature and, sometimes, eroded by
256 ooid layers. Ooids occasionally are notable by their “ghost” texture, probable resulting
257 from dissolution during diagenesis (Fig. 11). In the examination under the fluorescence
258 microscope, dark-coloured laminae show intense fluorescence when comparing with non-
259 and very weak fluorescence within light-coloured layers (Fig. 12).

260

261 SEM analysis reveals that the cortices of ooids are composed of micrite with an
262 internal fabric that ranges from distinctly concentrically laminated to homogenous and
263 dense (Fig. 13). Ooids are commonly rimmed by bladed cement and between the ooids’
264 space, is occluded by blocky calcite cement (Fig. 13A–B). Ooid nuclei are usually
265 comprised of sparry dolomite, and the dolomite nuclei have distinct contact with outer
266 micritic layers (Fig. 13C–E). At magnifications of 130,000 \times and greater, nanometer-scale
267 features were readily observed within dolomite rhombs (Fig. 13F). These tiny particles
268 are spherical to ovate, isolated rod-shaped or lumpy-shaped, with diameter ranging from
269 50 nm to 200 nm (Fig. 13F).

269

270 **5. Discussion**

271

272 *5.1. Depositional environment of the stromatolite-oolite complex*

273

274 The Lichuan stromatolites grew initially either on grainstone or oolitic limestone in
275 shallow, below the wave-swept shoals on a carbonate platform (Fig. 2). Substratum
276 oolites represent agitated conditions, which prejudiced construction of stromatolite.

277 Strong water currents even physically eroded stromatolite underneath. When
278 environmental conditions became hospitable for microbes to settle on either ooid grains
279 or relative palaeo-highs of oolitic sea floor, they grew stromatolites. Modern domal
280 stromatolites with the best lamination in Hamelin Pool of Shark Bay, Western Australia,
281 grow under the mean tidal surface (Suosaari et al., 2016). The Lichuan giant stromatolites
282 are even more densely built than modern stromatolites (Fig. 4), and thus indicate a
283 slightly higher (or lower) energy habitat than the Shark Bay stromatolites.

284

285 *5.2. Biogenic origin and geobiologic processes associated with accretion of the Lichuan*
286 *stromatolites*

287

288 *5.2.1. Lithification of microbial microstructures in stromatolites*

289

290 The Lichuan stromatolites show a wide variety of microfabrics. Of these, the most
291 common microbial lamination type is the diffuse laminated microstructure. Enlargement
292 of diffuse dark laminae displays diffusively clotted or reticular structures, which have
293 irregular boundaries to the adjacent light-coloured areas. Similar microstructures have
294 also been observed from the Neoproterozoic stromatolite deposits of the Beck Spring
295 Dolomite, ranging from distinct to diffusively laminated/clotted structures (Harwood and
296 Summer, 2012). The diffusively clotted structures are thought to have resulted from the different
297 timing of lithification relative to the growth and decay of the microbial communities. The
298 distinct laminated/clotted structures may have originated from an early cementation of
299 microbial communities with minimal degradation, whereas the diffusively
300 laminated/irregularly clotted structures may have resulted from an early degradation of
301 microbial communities and later cementation (Harwood and Sumner, 2012). Such
302 interpretation is also plausible for the formation of diffusively clotted microclots in the Lichuan
303 stromatolite. The Lichuan reticular microstructures are similar to reticulate microfabrics
304 in stromatolites near the Permian–Triassic boundary in Hungary (Hips and Haas, 2006).
305 The reticulate appearance of these laminae was interpreted to be attributed to winnowing
306 of mat particles by weak currents (Hips and Haas, 2006). These microfabrics appear to be
307 cavernous (Fig. 6C), and the dark-coloured filiform micrite probably represents calcified
308 extracellular polymeric secretions (EPS), and/or the filiform micrite itself may represent
309 mucus or biofilms generated by microbes (Noffke et al., 2003). The pronounced clotted
310 structures of the Lichuan stromatolites are similar to Peloid-A2.2 defined by Adachi et al.
311 (2004). The latter were possibly formed through calcification of assemblage (colony) of
312 coccoidal microbes and/or by the aggregation of smaller individual peloids (Adachi et al.,
313 2004).

314

315 *5.2.2 Biogenic related minerals in Lichuan stromatolite*

316

317 SEM imaging unravels the common occurrence of nanometer-scale textures relative
318 to the formation of the dolomite and to move forward, relative to microbial activities.
319 Moreover, ubiquitous occurrence of authigenic microquartz crystals in association with
320 clay minerals implies that the formation of micro-quartz crystals is attributed to microbial
321 reduction by sulfate reducing bacteria (RSB) (Luo et al., 2016).

322

Some modern examples suggest that microbial sulphate reduction under anoxic

323 conditions can promote dolomite precipitation by removing sulphate and reducing the
324 kinetic inhibition of dolomite formation (Warthmann et al., 2000; Wright and Wacey,
325 2005; Krause et al., 2012). Several lines of evidence indicate the existence of the
326 SRB-induced microbial formation of dolomite in the Lichuan stromatolite. As described
327 above, the Lichuan stromatolite has abundant nano-sized lumpy-shaped textures that
328 form amorphous aggregates. Comparable structures were also reported by Gournay et al
329 (1999), who interpreted such nanometer-scales textures, in dolomite surface, precipitated
330 in organic-rich, bacterial environment.

331 Moreover, authigenic quartz grains in conjunction with minute rhombic moulds are
332 also rather abundant in stromatolitic laminae. The formation of euhedral quartz crystals
333 has been interpreted as a result of lowered pH value by sulfide oxidizing, in which sulfide
334 was produced by sulfate reduction (Chafetz and Zhang, 1998). As a result, the growth of
335 euhedral authigenic quartz may indicate the bacteria sulfate reduction and sulfide
336 oxidation processes (Friedman and Shukla, 1980). Some platy clay minerals attached to
337 authigenic quartz surfaces or occluded within amorphous quartz crystals (Fig. 8D). These
338 quartz crystals show no sign of abrasion on crystal surface, thus precluding a detrital
339 origin and transportation. But it should also be noted that the possibility that those
340 euhedral quartz grains originated from volcanism cannot be ruled out because volcanic
341 eruptions have also produced many morphologically same authigenic quartz recorded in
342 the P–Tr boundary successions in South China (Yin et al., 1992; Gao et al., 2013).

343

344 *5.3. Biogenetic origin and geobiologic process associated with formation of Lichuan* 345 *ooids*

346

347 Giant ooids have been widely reported from the P–Tr boundary beds worldwide (Li
348 et al., 2013, 2015). The main controls on the generation of giant ooids are attributed to
349 reduced nucleus supply, increased growth rate, and higher environmental energy levels
350 (Sumner and Grotzinger, 1993). Lower supply of skeletal grains means reduced supply of
351 nuclei. What's more, the absence of a dominant skeletal sink of calcium carbonate
352 influences both regional carbonate saturation state and local carbonate removal
353 mechanism (Payne et al., 2006). Growth rate of ooids highly relies on carbonate
354 saturation state (Sumner and Grotzinger, 1993). Environmental energy levels are
355 commonly high in oolitic facies. Carbonate ramps possess unprotected margins that allow
356 waves and currents to create more agitated conditions along the shallow water facies,
357 forming a narrow ooid band on the Yangtze carbonate platform (Fig. 2). Only when the
358 energy threshold needed to put in motion an ooid of a given size is exceeded,
359 mobilization and growth of ooids can occur. Giant ooid usually have larger energy
360 thresholds than normal ooid (Heller et al., 1980). Episodic hydrodynamic events such as
361 storms, occasional strong tidal wave, and gale wind, may cause higher energy condition,
362 leading to formation, destruction, and/or re-cementation of giant ooids (Fig. 10D). Such a
363 process would be repetitive as long as the mass of ooid grains can float under highest
364 energy condition. Stromatolite-oolite complex may indicate alternating appearance of
365 high and low energy conditions.

366

367 The origin of dolomite has long been enigmatic mainly due to its common
368 occurrences in ancient rocks but rare presence in modern marine environment (Arvidson
and MacKenzie, 1999). Microbial mediation during dolomite formation potentially

369 resolves this long-stand debate (Vasconcelos and McKenzie, 1997; Burne et al., 2000).
370 Dolomitization is very common in various Lichuan ooid grainstones, and dolomite shows
371 abundant nanometer-scale structures that resemble those observed by Gournay et al
372 (1999). These features provided corroborating evidence for the formation of dolomite in
373 organic-rich environments under near-surface conditions (Gournay et al., 1999). Culture
374 experiments by Warthmann et al. (2000) demonstrated that modern species of
375 sulfate-reducing bacteria are capable of mediating dolomite formation in a synthetic
376 anoxic hypersaline habitat. Typical dumbbell-shaped dolomites appear to be uniquely
377 mediated by sulfate reducing microbes (Warthmann et al., 2000). Though no
378 dumbbell-shaped objects are detected in the Lichuan ooids and stromatolites, similar size
379 amorphous nano-scale dolomite may also have genetic relationship to sulfate reducing
380 microbes.

381

382 *5.4. Growth and environmental stress of the Lichuan giant stromatolite*

383

384 Modern stromatolite is reported from the brackish waters of Lake Clifton of Western
385 Australia, the hypersaline waters of Hamelin Pool in Shark Bay, and the open marine
386 environments of the Bahamas (Andres et al., 2006; Morse et al., 1984). Similarities
387 between the Lichuan stromatolites and modern “giant” stromatolites are striking. They
388 are comparable in size and general morphology, in possessing both broad convex-up
389 lamination and large columnar structures (Figs 4–5). Moreover, the Lichuan stromatolites
390 show constructing as well as destructing structures (Fig. 4D–E) that are surrounded by
391 ooid shoal deposits. The Lichuan stromatolite colonized broad, essentially oolitic
392 substrates, and this may account for their less steep sided, typically domical shape.

393 Lichuan stromatolite also provides insights into the ecology of ancient microbial
394 communities. Microbial calcite producing communities flourished as higher organisms
395 were nearly absent due to rapidly changing environmental condition or the sequelae of
396 the Permian–Triassic mass extinction. Stromatolites and oolites bearing beddings of the
397 Upper Daye Formation are nearly devoid of fossils, body fossils as well as trace fossils.
398 The reason of this scarceness may be rapidly changing environmental conditions as the
399 shallow and belt-like seacoast has no buffering capacity against fluctuations of various
400 environmental parameters. The etched surfaces of the top of the stromatolites resulted
401 from the wave’s washing against the stromatolites, leaving stromatolite fragments
402 re-deposited in the interval between columns of stromatolites (Fig. 4E). Some
403 prerequisites of stromatolitic growth can be deduced from observations in the field. Wave
404 strength and mud content are the main influence factors on the formation of stromatolites.
405 On one hand, high energy conditions are preference to the formation of ooids, even giant
406 ooids, and prejudice to the formation of stromatolites. On the other hand, high mud
407 content water or mud layers excluded stromatolites or terminated their growth. The
408 microbial community did not survive a mud coverage or muddy water. This effect may
409 be the reason for their restriction to the distribution only on the oolitic shore of the Upper
410 Daye Formation. The mud banded limestone of the overlying Jialingjiang Formation
411 indicates high mud content in seawater, which terminated the deposit of oolites and
412 stromatolites.

413 Protective stress to deter competitors will promote stromatolite growth (Chen and
414 Benton, 2012) and may be provided by a variety of factors, including hypersalinity

415 (Garrett, 1970) or mobile-sediment (Dravis, 1983). These are not mutually exclusive and
416 could act together. The Lichuan stromatolites appear to have grown in a normal open
417 marine setting (Fig. 2). The environmental stress is probably mainly caused by strong
418 tidal currents and the resultant ooids sand-waves which periodically engulf the
419 stromatolites.

420

421 *5.5. Implications for the Early Triassic extended environmental stress and microbial* 422 *bloom*

423

424 Early Triassic stromatolites have been reported widely from around the world (Sano
425 and Nakashima, 1997; Richoz et al., 2005; Hips and Haas, 2006; Pruss et al., 2006;
426 Kershaw et al., 2011; Chen et al., 2012, 2014; Mata and Bottjer, 2012; Luo et al., 2016).
427 In particular, the Permian–Triassic boundary microbialites (PTBMs) were widely
428 distributed in low-latitude shallow-marine carbonate shelves in central Tethyan
429 continents (Yang et al., 2011; Kershaw et al., 2012). Some biogeochemical signals
430 mirroring various microbial communities associated with benthic microbial mats have
431 been detected from diagenetic carbonate crystal fan deposits of Dienerian–Smithian age
432 (Heindel et al., 2014). Thus, microbes existed widely in various niches of the
433 post-extinction oceans. Different stages of the Early Triassic stromatolites may have
434 different microbial compositions and cause of formation. Ezaki et al. (2012) documented
435 an Olenekian stromatolite from South China and considered that it grew in the
436 inhospitable anoxic/sulfidic marine conditions. In contrast, the Smithian stromatolite
437 from the Perth Basin, Western Australia grew in an oxic condition (Chen et al., 2014).

438 The resurgence of microbialites was throughout the Early–Middle Triassic, they
439 were suggested to proliferate particularly in six intervals: earliest Griesbachian, late
440 Griesbachian–early Dienerian, early Smithian, late Smithian, late Spathian, and early
441 Anisian, respectively (Baud et al., 2005, 2007; Pruss et al., 2006; Mata and Bottjer, 2012;
442 Chen et al., 2014; Luo et al., 2014, 2016). Of these, the PTBMs are most widespread
443 among all Early Triassic microbialites (Kershaw et al., 2012). Copious coccoid-like
444 objects, presumed to be cynaobacteria were found in the PTBMs from Sichuan and
445 Guizhou Provinces, South China (Ezaki et al., 2003, 2008; Wang et al., 2005). Similar
446 calcispheroids have also been reported from the P–Tr stromatolites in the Chongyang
447 area, Hubei Province, South China (Yang et al., 2008, 2011) and Bükk Mountains of
448 Hungary (Hips and Haas, 2006). The similarity in microbial composition possibly
449 suggests a similar microbial metabolism mechanism inducing the growth of these PTBMs.
450 However, microbialites in other intervals of the Early Triassic preserve different microbes
451 such as coccoid-like objects, bacterial clump-like spheroids, ‘*Gakhumella*’, and *Renalcis*
452 of the earliest and late Early Triassic microbialites (Lehermann, 1999; Ezaki et al., 2003,
453 2008, 2012; Wang et al., 2005; Yang et al., 2008, 2011; Wu et al., 2014; Luo et al., 2016;
454 Fang et al., 2016), filament sheaths in Smithian stromatolite (Chen et al., 2014), and
455 fossilized filamentous cyanobacteria sheath in early Anisian (Luo et al., 2014).

456 The Lichuan stromatolite is interpreted to be formed from the activity of SRB or
457 oxygenic phototrophic bacteria, whose microbial composition was largely controlled by
458 inhospitable anoxic/sulphidic marine conditions that prevailed in the Early Triassic
459 oceans (Ezaki et al., 2012; Huang et al., 2016). In this regard, the Lichuan stromatolite
460 might also represent a regional sedimentary response to the microbial proliferation during

461 the Smithian. The post-extinction hash environments therefore may have continued to
462 exist or even expanded in shallow marine in South China during the Smithian (Huang et
463 al., 2016). A few microbialites of Early Triassic age have also been reported from
464 western US and Oman (Woods and Baud, 2008; Woods, 2009, 2014), but it is not yet
465 clear whether these microbialite deposits have similar geobiologic features to those
466 reported by Ezaki et al. (2012) or Chen et al. (2014). In addition, stack pattern of
467 ooid-stromatolite complex in Lichuan is similar to those coeval deposits in Germanic
468 basin, implying the worldwide proliferation of microbes during Early Triassic period.

469

470 **6. Conclusions**

471

472 A unique massive stromatolite, probably the known thickest Early Triassic
473 stromatolite deposit developing in association with giant ooid banks is described from the
474 middle Lower Triassic (late Smithian) of the Lichuan area, western Hubei Province,
475 South China. The stromatolites are up to 18 m high and exhibit various growing forms
476 including domical, stratified columnar, wavy laminated, cabbage-shaped, roll-up, and
477 conical structures. Under the optical microscope, stromatolite laminations are
478 conspicuous and usually consist of diffuse laminated, reticular, intraclastic, and irregular
479 distinct clotted microstructure. The SEM imaging reveals that the common occurrence of
480 nanometer-scale textures relative to the formation of the dolomite both in stromatolite
481 and ooid, as well as authigenic quartz grains commonly preserving in stromatolite, could
482 be attributed to abundant organic matters in seawater. Thick giant stromatolite provides
483 us with invaluable insight into Early Triassic oceanic conditions. Microbes were probably
484 extremely flourishing in both eastern and western margins of the Palaeo-Tethys Ocean
485 during middle Early Triassic, suggesting the worldwide long-term degradation of marine
486 ecosystems after the end-Permian extinction.

487

488 **Acknowledgement**

489 This study is partly supported by the 111 Program of China (B80210), three
490 research grants from the State Key Laboratory of Biogeology and Environmental
491 Geology (BGEG), and State Key Laboratory of Geological Processes and Mineral
492 Resources, China University of Geosciences (GBL11206 and GPMR201302), and two
493 NSFC grants (41272023, 41572091). It is a contribution to the IGCP 630
494 “Permian–Triassic extreme climate and environment”

495

496

497 **References**

498

499 Adachi, N., Ezaki, Y., Liu, J.B., 2004. The fabrics and origins of peloids immediately
500 after the end-Permian extinction, Guizhou Province, South China. *Sediment. Geol.*
501 164, 161–178.

502 Andres, S., Miriam, T., Reid, R.P., Pamela, R.R., 2006. Growth morphologies of modern
503 marine stromatolites: A case study from Highborne Cay, Bahamas. *Sediment. Geol.*

504 185, 319–328

505 Arvidson, R.S., and MacKenzie, F.T., 1999, The dolomite problem: Control of
506 precipitation kinetics by temperature and saturation state. *Am. J. Sci.* 299, 257–288.

507 Baud, A., Richoz, S., Marcoux, J., 2005. Calcimicrobial cap rocks from the basal Triassic
508 units: western Taurus occurrences (SW Turkey). *Comptes Rendus Palevol* 4, 501–514.

509 Baud, A., Richoz, S., Pruss, S., 2007. The Lower Triassic anachronistic carbonate facies
510 in space and time. *Glob. Planet. Chang.* 55, 81–89.

511 Burne, S.J., McKenzie, J.A., Vasconcelos, C., 2000. Dolomite formation and
512 biogeochemical cycles in the Phanerozoic. *Sediment. Geol.* 47, 49–61.

513 Chafetz, H.S., Zhang, J., 1998. Authigenic euhedral megaquartz crystals in a Quaternary
514 dolomite. *J. Sediment. Res.* 68, 994–1000.

515 Chen, Z.Q., Benton, M.J., 2012. The timing and pattern of biotic recovery following the
516 end-Permian mass extinction. *Nat. Geosci.* 5, 375–383.

517 Chen, Z.Q., Wang, Y.B., Kershaw, S., Luo, M., Yang, H., Zhao, L.S., Fang, Y.H., Chen,
518 J.B., Li, Yang., Zhang, L., 2014. Early Triassic stromatolites in a siliciclastic
519 nearshore setting in northern Perth Basin, Western Australia: geobiologic features and
520 implications for post-extinction microbial proliferation. *Glob. Planet. Chang.* 121,
521 89–100.

522 Dravis, J.J., 1983. Hardened subtidal stromatolites, Bahamas. *Science* 219, 385–386.

523 Erwin, D.H., 2006. *Extinction: How Life on Earth Nearly Ended 250 Million Years Ago.*
524 Princeton University Press, Princeton, pp. 1–296.

525 Ezaki, Y., Liu, J.B., Adachi, N., 2003. Earliest Triassic microbialite micro- to
526 megastructures in the Huaying area of Sichuan Province, South China: implications
527 for the nature of oceanic conditions after the end-Permian extinction. *PALAIOS* 18,
528 388–402.

529 Ezaki, Y., Liu, J.B., Adachi, N., 2012. Lower Triassic stromatolites in Luodian County,
530 Guizhou Province, South China: evidence for the protracted devastation of the marine
531 environments. *Geobiology* 10, 48–59.

532 Feng, Z.Z., Bao, Z.D., Li, S.W., 1997. *Lithofacies Paleogeography of Early and Middle*
533 *Triassic of South China.* Petroleum Industry Press, Beijing, pp. 1–222 (in Chinese).

534 Friedman, G.M., Shukla, V., 1980. Significance of Authigenic Quartz Euhedra After

535 Sulfates: Example From the Lockport Formation (Middle Silurian) of New York. J.
536 Sediment. Res. 50. 1299–1304.

537 Garrett, P., 1970. Phanerozoic stromatolites: noncompetitive ecologic restriction by
538 grazing and burrowing animals. Science 169, 171–173.

539 Gournay, J.P., Kirkland, B.L., Folk, R.L., Lynch, F.L., 1999. Nanometer-scale features in
540 dolomite from Pennsylvanian rocks, Paradox Basin, Utah. Sediment. Geol. 126,
541 243–252.

542 Kershaw, S., Crasquin, S., Forel, M.B., Randon, S., Collin, P.Y., Kosun, E., Richoz, S.,
543 Baud, A., 2011. Earliest Triassic microbialites in Çürük Dag, southern Turkey:
544 composition, sequence and controls on formation. Sedimentol. 58, 739–755.

545 Kershaw, S., Crasquin, S., Li, Y., Collin, P.Y., Forel, M.B., Mu, X.N., Baud, A., Wang,
546 Y., Xie, S.C., Maurer, F., Gou, L., 2012. Microbialites and global environmental
547 change across the Permian–Triassic boundary: a synthesis. Geobiology 10, 25–47.

548 Li, F., Yan, J. X., Algeo, T., Wu, X., 2013. Paleooceanographic conditions following the
549 end-Permian mass extinction recorded by giant ooids (Moyang, South China). Glob.
550 Planet. Chang. 105, 102–120.

551 Li, F., Yan, J., Chen, Z.-Q., Ogg, J. G., Tian, L., Korngreen, D., Liu, K., Ma, Z., and
552 Woods, A. D., 2015, Global oolite deposits across the Permian–Triassic boundary: A
553 synthesis and implications for palaeoceanography immediately after the end-Permian
554 biocrisis. Earth-Sci. Rev. 149, 163–180.

555 Luo, M., Chen, Z.Q., Zhao, L.S., Kershaw, S., Huang, J.Y., Wu, L.L., Yang, H., Fang,
556 Y.H., Huang, Y.G., Zhang, Q.Y., Hu, S.X., Zhou, C.Y., Wen, W., Jia, Z.H., 2014.
557 Early Middle Triassic stromatolites from the Luoping area, Yunnan Province,
558 Southwest China: geobiologic features and environmental implications. Palaeogeogr.
559 Palaeoclimatol. Palaeoecol. 412, 124–140.

560 Luo, M., Chen, Z.Q., Shi, G.R., Fang, Y.H., Song, H.J., Jia, Z.H., Huang, Y.G., Hao, Y.,
561 2016. Upper Lower Triassic stromatolite from Anhui, South China: geobiologic
562 features and palaeoenvironmental implications. Palaeogeogr. Palaeoclimatol.
563 Palaeoecol. 452, 40–54.

564 Mata, S.A., Bottjer, D.J., 2012. Microbes and mass extinctions: paleoenvironmental
565 distribution of microbialites during times of biotic crisis. Geobiology 10, 3–24.

566 Mei, M.X., 2008. Implication for the unusual giant oolites of the Phanerozoic and their
567 morphological diversity: a case study from the Triassic Daye Formation at the Lichuan
568 Section in Hubei Province, South China. *Geosci.* 22, 683–698 (In Chinese with
569 English abstract).

570 Morse J. W., Millero F. J., Thurmond V., Brown E., and Ostlund H. G. (1984) The
571 chemistry of Grand Bahama Bank waters: After 18 years another look. *J. Geophys.*
572 *Res. Oceans* 89, 3604–3614.

573 Payne, J.L., Lehrmann, D.J., Wei, J., Knoll, A.H., 2006. The pattern and timing of biotic
574 recovery from the end-Permian extinction on the Great Bank of Guizhou, Guizhou
575 Province, China. *PALAIOS* 21, 63–85.

576 Pruss, S.B., Bottjer, D.J., Corsetti, F.A., Baud, A., 2006. A global marine sedimentary
577 response to the end-Permian mass extinction: examples from southern Turkey and the
578 western United States. *Earth-Sci. Rev.* 78, 193–206.

579 Harwood, C.L., Sumner, D.Y., 2012. Origins of microbial microstructures in the
580 Neoproterozoic Beck Spring Dolomite: variations in microbial community and timing
581 of lithification. *J. Sediment. Res.* 82, 709–722.

582 Heindel, K., Richo, S., Birgel, D., Brandner, R., Klugel, A., Krystyn, L., Baud, A., Horacek,
583 M., Mohtat, T., Peckmann, J., 2014. Biogeochemical formation of calyx-shaped
584 carbonate crystal fans in the subsurface of the Early Triassic seafloor. *Gondwana Res.*
585 [http:// dx.doi.org/10.1016/j.gr.2013.11.004](http://dx.doi.org/10.1016/j.gr.2013.11.004).

586 Heller, P.L., Komar, P.D., Pevear, D.R., 1980. Transport processes in ooid genesis. *J.*
587 *Sediment. Res.* 50, 943–951.

588 Hips, K., Haas, J., 2006. Calcimicrobial stromatolites at the Permian–Triassic boundary
589 in a western Tethyan section, Bükk Mountains, Hungary. *Sediment. Geol.* 185,
590 239-253.

591 Noffke, N., Gerdes, G., Klenke, Th., 2003. Benthic cyanobacteria and their influence on
592 the sedimentary dynamics of peritidal depositional systems (siliciclastic, evaporitic
593 salty and evaporitic carbonatic). *Earth-Sci. Rev.* 12, 1–14.

594 Richo, S., Baud, A., Krystyn, L., Twitchett, R., Marcoux, J., 2005. Permo–Triassic
595 deposits of the Oman Mountains: from basin and slope to the shallow platform. Field
596 guidebook. 24th IAS Regional Meeting, Oman.

597 Saito, R., Kaiho, K., Oba, M., Fujibayashi, M., Tong, J.N., Tian, L., 2015. Predominance
598 of Archaea-derived hydrocarbons in an Early Triassic microbialite. *Org. Geochem.* 85,
599 66–75.

600 Sano, H., Nakashima, K., 1997. Lowermost Triassic (Griesbachian) microbial
601 bindstone–cementstone facies southwest Japan. *Facies* 36, 1–24.

602 Shapiro, R.S., 2000. A comment on the systematic confusion of thrombolites. *PALAIOS*
603 15, 166–169.

604 Song, H.J., Wignall, P.B., Tong, J.N., Bond, D.P.G., Song, H.Y., Lai, X.L., Zhang, K.X.,
605 Wang, H.M., Chen, Y.L., 2012. Geochemical evidence from bio-apatite for multiple
606 oceanic anoxic events during Permian–Triassic transition and the link with
607 end-Permian extinction and recovery. *Earth Planet. Sci. Lett.* 353–354, 12–21.

608 Sumner, D.Y., Grotzinger, J.P., 1993. Numerical modeling of ooid size and the problem
609 of Neoproterozoic giant ooids. *J. Sediment. Res.* 63, 974–982.

610 Suosaari, E.P., Reid, R.P., Playford, P.E., Foster, J.S., Stolz, J.F., Casaburi, G., Hagan,
611 P.D., Chirayath, V., Macintyre, I.G., Planavsky, N.J. Eberli, G.P., 2016. New
612 multi-scale perspectives on the stromatolites of Shark Bay, Western Australia. *Sci.*
613 *Rep.* 6, 1–13.

614 Vasconcelos, C.O., McKenzie, J.A., 1997. Microbial mediation of modern dolomite
615 precipitation and diagenesis under anoxic conditions (Lagoa Vermelha, Rio de Janeiro,
616 Brazil). *J. Sediment. Res.* 67, 378–390.

617 Wang, Y.B., Tong, J.N., Wang, J.S., Zhou, X.G., 2005. Calcimicrobialite after
618 end-Permian mass extinction in South China and its palaeoenvironmental significance.
619 *Chin. Sci. Bull.* 50, 7665–7671.

620 Wang, Z.H., Cao, Y.Y., 1981. Early Triassic conodonts from Lichuan, western Hubei.
621 *Acta Palaeontol. Sin.* 20. 363–375 (In Chinese with English abstract).

622 Warthmann, R., van Lith, Y., Vasconcelos, C., McKenzie, J.A., Karpoff, A.-M., 2000.
623 Bacterially induced dolomite precipitation in anoxic culture experiments. *Geology* 28,
624 1091–1094.

625 Woods, A.D., Baud, A., 2008. Anachronistic facies from a drowned Lower Triassic
626 carbonate platform: lower member of the Alwa Formation (Ba'id Exotic), Oman
627 Mountains. *Sediment. Geol.* 209, 1–14.

- 628 Woods, A.D., 2009. Anatomy of an anachronistic carbonate platform: Lower Triassic
629 carbonates of the southwestern United States. *Aust. J. Earth Sci.* 56, 825–839.
- 630 Woods, A.D., 2014. Assessing Early Triassic paleoceanographic conditions via unusual
631 sedimentary fabrics and features. *Earth-Sci. Rev.* 137, 6–18.
- 632 Wu, Y.L., Zhu, H.F., Zhu, Z.F., Yan, Y.J., 1994. Triassic Lithofacies, Paleogeography
633 and Mineralization in South China. Geological Publishing House, Beijing. 28 pp. (in
634 Chinese with English abstract).
- 635 Yang, H., Wang, Y.B., Chen, L., 2008. Occurrence of organic matter in
636 calcimicrobialites across Permian–Triassic boundary in Huayingshan region, Sichuan,
637 South China. *J. China Univ. Geosci.* 19, 518–525.
- 638 Yang, H., Chen, Z.Q., Wang, Y.B., Tong, J.N., Song, H.J., Chen, J., 2011. Composition
639 and structure of microbialite ecosystems following the end-Permian mass extinction in
640 South China. *Palaeogeogr. Palaeoclimatol. Palaeoecol.* 308, 111–128.
- 641 Yin, H.F., Huang, S.J., Zhang, K.X., 1992. The effects of volcanism on the
642 Permo–Triassic mass extinction in South China. In: Sweet, W.C., Yang, Z.Y., Dickins,
643 J.M., Yin, H.F. (Eds), *Permo–Triassic Events in the Eastern Tethys*. Cambridge
644 University Press, London, pp. 146–157.
- 645 Zhao, L.S., Chen, Y.L., Chen, Z.Q., Gao, L., 2013. Uppermost Permian to Lower Triassic
646 conodont zonation from Three Georges area, South China. *PALAIOS* 28, 523–540.
- 647 Zhao, L.S., Orchard, M.J., Tong, J.N., Sun, Z.M., Zuo, J.X., Zhang, S.X., Yun, A.L.,
648 2007. Lower Triassic conodont sequence in Chaohu, Anhui Province, China and its
649 global correlation. *Palaeogeogr. Palaeoclimatol. Palaeoecol.* 252, 24–38.

650

651 **Figure captions**

652

653 **Fig. 1.** Location of the Lichuan section in the Lichuan City, western Hubei Province.
654 South China.

655 **Fig. 2.** Early Triassic palaeogeographic configurations of the upper Yangtze region
656 (modified from Wu et al., 1994). Transect from A to D indicates an eastward
657 progradational process. The original conodont zones follow Wang et al. (1981), and
658 modified based on those established from the uppermost Permian to Lower Triassic of

659 the neighboring Daxiakou section (Zhao et al., 2013). The stromatolite–oolite complex
660 developed in Smithian. Roman numerals represent different sedimentary facies: I,
661 swamp/fluvial facies; II, tidal-flat facies; III, lagoon facies; IV, tidal-flat facies; V,
662 oolitic beach; VI, ramp facies; VII, basin facies.

663 **Fig. 3.** Lithostratigraphy of the upper Daye Formation and the lower Jialingjiang
664 Formation at the Lichuan section. Conodont zones follow Wang et al. (1981).

665 **Fig. 4.** Field photos of the Daxiandong section. A, Well-exposed successions of the upper
666 Daye Formation and lower Jialingjiang Formation. The person in the center is 1.6
667 meter high. Stromatolites have been sliced by vertical plane. B–C, Vertical sections
668 of stromatolite in the middle beddings, show domical structure. Domical stromatolites
669 are closely packed. D, Vertical sections of stromatolite in the middle beddings, shows
670 upward growth morphology and seemingly branching of a single stromatolite dome. E,
671 Vertical sections of stromatolite in the Upper part and the top of the domical
672 stromatolite (Dom) was eroded and surrounded by oolitic sands (OS). Stromatolite
673 was destructed and the fragments were re-deposited aside the stromatolite column
674 (arrows indicate the boundary of domical stromatolite and oolitic sands). Color in D, F
675 is processed by Adobe Photoshop CS6.

676 **Fig. 5.** Field photos showing macro-structures of the stromatolite. A, Wavy laminated
677 stromatolite shown on the vertical dimension. B, Vertical section of cabbage-shaped
678 stromatolite. C, Field view showing laminated and roll-up structures of stromatolite. D,
679 Vertical section of stromatolite showing lateral extension feature. E, Domical
680 stromatolite showing distinct laminae. F, Sharply peaked conical forms stromatolite in
681 vertical section.

682 **Fig. 6.** Photomicrographs of the Lichuan cabbage-shaped stromatolite, plane-polarized
683 light. A, Transmitted photo of stromatolite laminae on vertical profile. Note the dark
684 colored diffusive laminae alternating with light colored laminae, and dark colored
685 diffusive laminae are wavy and clotted in some part. B, Close-up of boxed area on the
686 upper left in A, showing reticular microstructures in lamina. C, Closed-up of boxed area
687 in B showing detailed reticular microstructures, which made up of micrite or opaque
688 materials.

689 **Fig. 7.** Photomicrographs of the Lichuan stromatolite, plane-polarized light. A–B,

690 different scale of reticular microstructures. A, There is intergradation between dark
691 laminated/reticular structures and light colored sparry calcite, highlighted by deep red
692 color. Color is processed by Adobe Photoshop CS6. B, Reticular microstructures
693 showing arc-shaped or forming semi-circle and constructing chamber-like structures.
694 C–D, Intraclastic microstructure. The honey colored sparry dolomite forming irregular
695 intraclasts. Noted the poor roundness and in some place, edge of intraclasts is sharp.
696 Matrix shows vein-like shape. E, Irregular distinct clotted microstructures. Individual
697 dark rounded microclots are densely spaced. F, Enlargement of distinct clots.
698 Individual dark rounded microclots are visible at the outer margin mesoclots where
699 they are less densely packed.

700 **Fig. 8.** Thin section photomicrograph and SEM photomicrographs of Lichuan stromatolite.
701 A, Plane-polarized transmitted light showing intraclastic microstructure (dol =
702 dolomite). B, BSE image of the same area in A. Darker area shows dolomite clumps.
703 C, Distributions of magnesium of the same area in B. D, Micro-quartz crystal within
704 stromatolite laminae. Note the platy clay minerals (arrows) are enwrapped within
705 micro-quartz grains. E, Enlargement of the dolomite crystals surface in B. Note the
706 surface of the dolomite has irregular to curdled texture. F, Nano-scale surface structure
707 of the dolomite in E. Lumpy-shaped (arrow) nanometer-scale textures.

708 **Fig. 9.** Field photographs of ooids at Lichuan section. A, Samples from the field of the
709 lowest bed 7 show thin laminae and ooids laminations. B, Oolitic grainstone
710 composed of giant ooids (orange arrow) with locally oolite intraclasts (red arrow). The
711 sample was etched by diluted hydrochloric acid. C, Weathering surface of oolitic
712 grainstone from the bed 2.

713 **Fig. 10.** Photomicrographs of ooids at Lichuan section, plane-polarized light. A, Ooids
714 show fine psephicity but relatively poor sorting. B–C, Giant ooids displaying
715 concentric laminae, recrystallized (dolomite-spar) nuclei (B). Note giant ooids with
716 selectively dolomitization laminae (arrow). D, Fragmentized ooids with outer sealed
717 cortices. E–F, Compound ooids. Smaller ooids and other grains are frequently
718 cemented together to form aggregate grains that may be bound together by laminated
719 micrite.

720 **Fig. 11.** Thin section photomicrograph of sample in figure 9A, plane-polarized light.

721 Ooids layers alternate with relatively dark layers. Dark layers between two ooids
722 layers are characterized by their stratified feature, similar to those in stromatolites.
723 Note that the distinct dark and light colored laminae in the middle. Ooids in the lower
724 part of the thin section are notable by their “ghost” texture, probable resulting from
725 dissolution during diagenesis. Ooids in the upper part are relatively well-preserved.
726 Note the erosion of dark laminae by ooids (arrow).

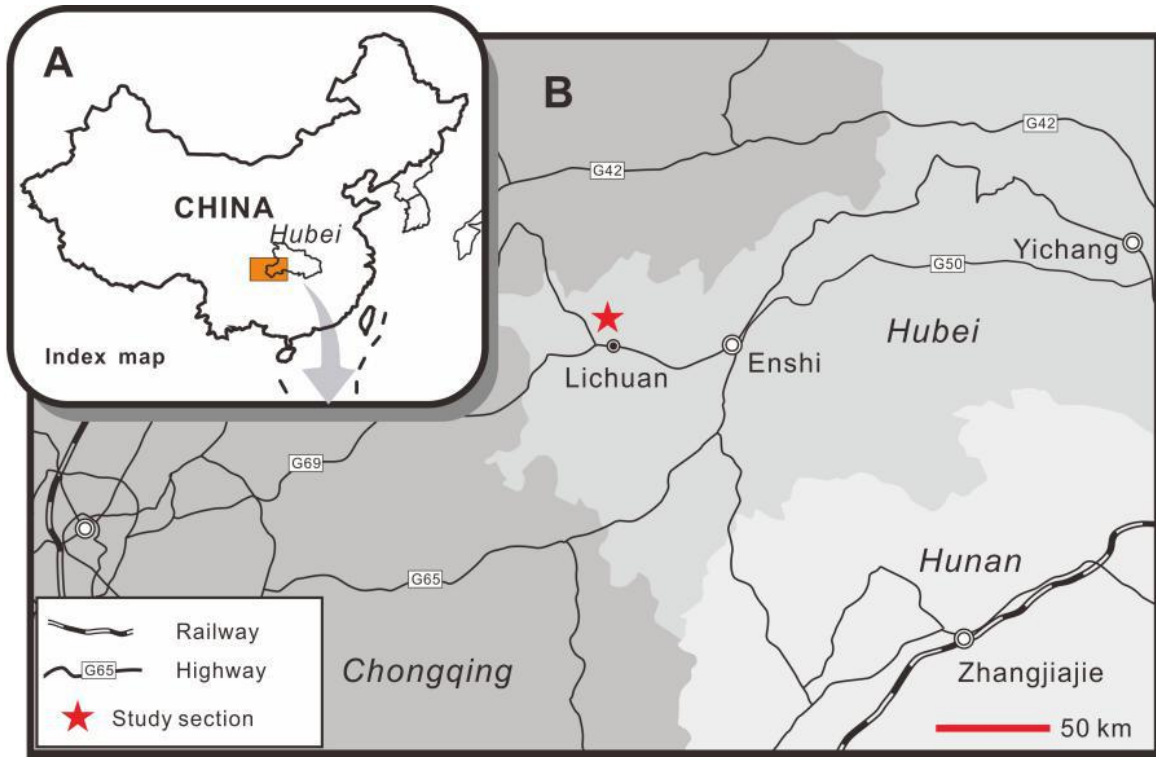
727 **Fig. 12.** Ooids in plane-polarized transmitted light (A–C) and different wavelengths of
728 fluorescent light under different exciting light (A1–C1, A2–C2, A3–C3). Blue
729 fluorescence (A1–C1, wavelength of 460–490 nm) is excited by exciting light that has
730 wavelength ranging from 330 nm to 380 nm; Green to light yellow fluorescence
731 (A2–C2, wavelength 510–540 nm) is excited by exciting light that has wavelength
732 ranging from 450 nm to 490 nm; Red fluorescence (A3–C3, wavelength 630 nm–660
733 nm) is excited by exciting light that has wavelength of 510–560 nm. Note that dark
734 laminae in all ooids samples are all actively responding to exciting light, while
735 coarse-grained dolomite or calcite cement is poorly responded to fluorescent light.

736 **Fig. 13.** SEM photomicrographs highlighting microbial fabric and authigenic mineral in
737 giant-oid cortices. A, Fresh broken surface showing microstructures of ooids. The
738 ooids are rimmed by a short bladed cement phase (BL) and the pore space is
739 commonly occluded by blocky calcite cement (BC). B, Polished surface eroded by
740 diluted hydrochloric acid, showing ooids cortices and outer bladed cement (BL) and
741 blocky calcite cement (BC). C, Ooid with sparry dolomite nuclei. D, Enlargement of
742 the dolomite nuclei. Note the contact between dolomite and outer calcite is sharp. E,
743 Enlargement of the contact area. Note the surface of the dolomite has irregular to
744 curdled texture. F, Nano scale of surface of the dolomite in E. Note numerous isolated
745 rod-shaped and lumpy-shaped (arrow) nanometer-scale textures.

746 **Fig. 14.** Cartoon diagram showing growth and demise of the Lichuan stromatolite and
747 oolite in Smithian, corresponding to figure 2D. Stage (A): the Lichuan area was above
748 the fair weather wave base, and ooids started to growth. Stage (B): stromatolites
749 initiated on ooids or directly on soft sediment. Stromatolites are densely placed and
750 closely piled up. Environmental factors are probably the main reason for the thriving of
751 stromatolite. Stage (C): ooids developed on the top of the stromatolite. Stromatolites

752 ceased growth due to high energy conditions and erosion of stromatolite appeared.
753 Stage (D): Again, reoccurrence of environmental factors in favoring of stromatolite
754 growth. Thickness of stromatolites in this horizon is thinner than the former one. Stage
755 (E): ooids developed on the top of the stromatolite similar to stage C.

782 Figure 1

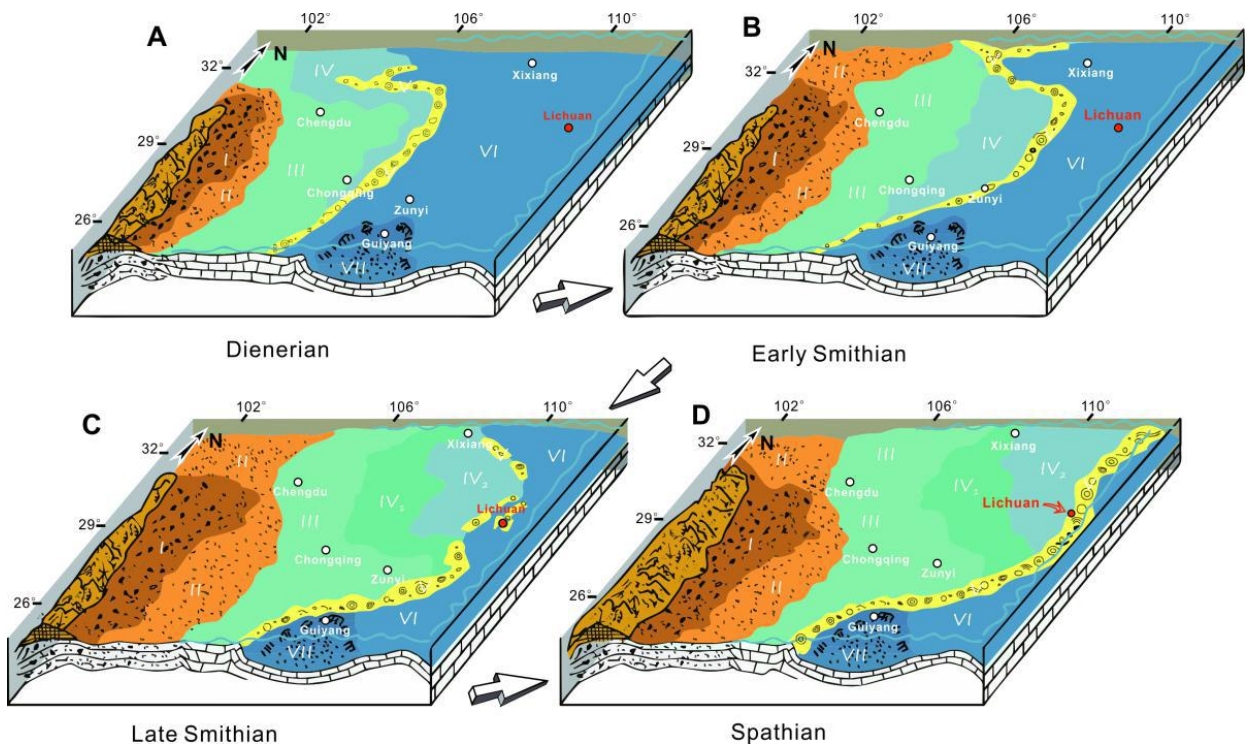


783

784

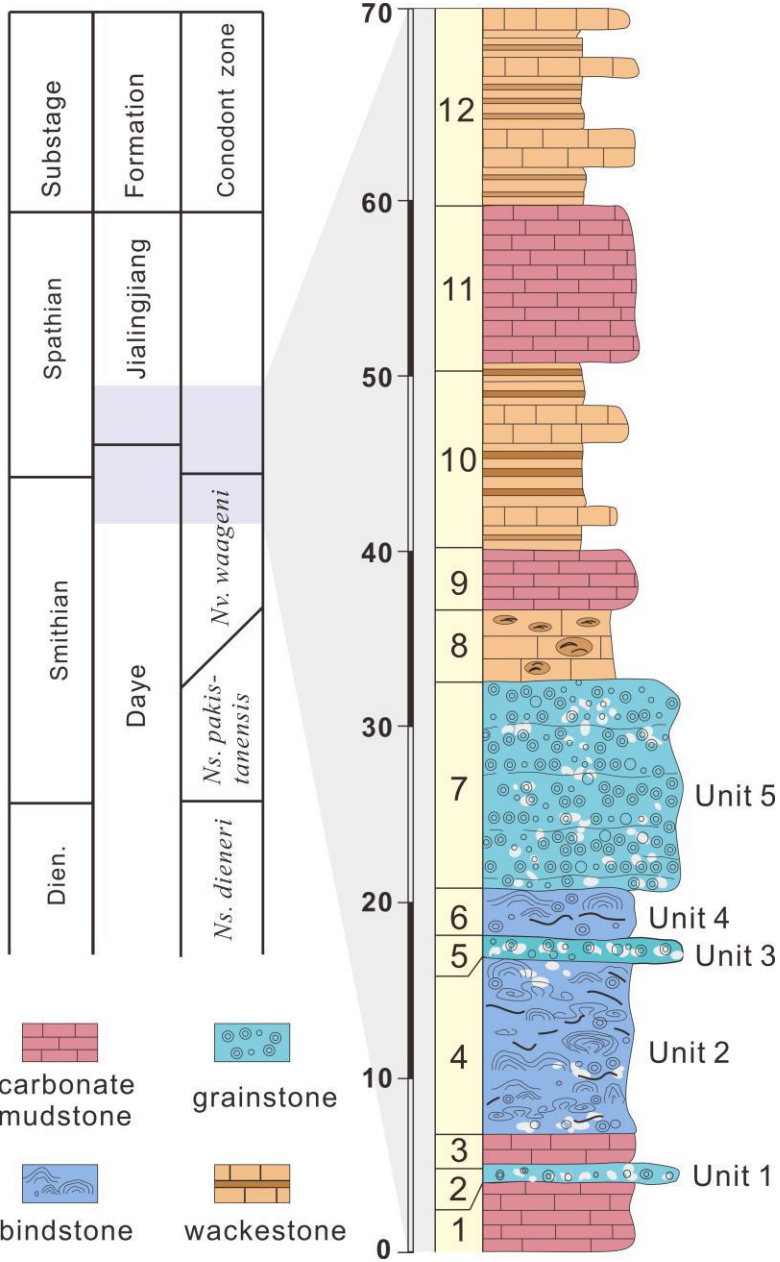
785

786 Figure 2



787

788 Figure 3



789

790

791

792

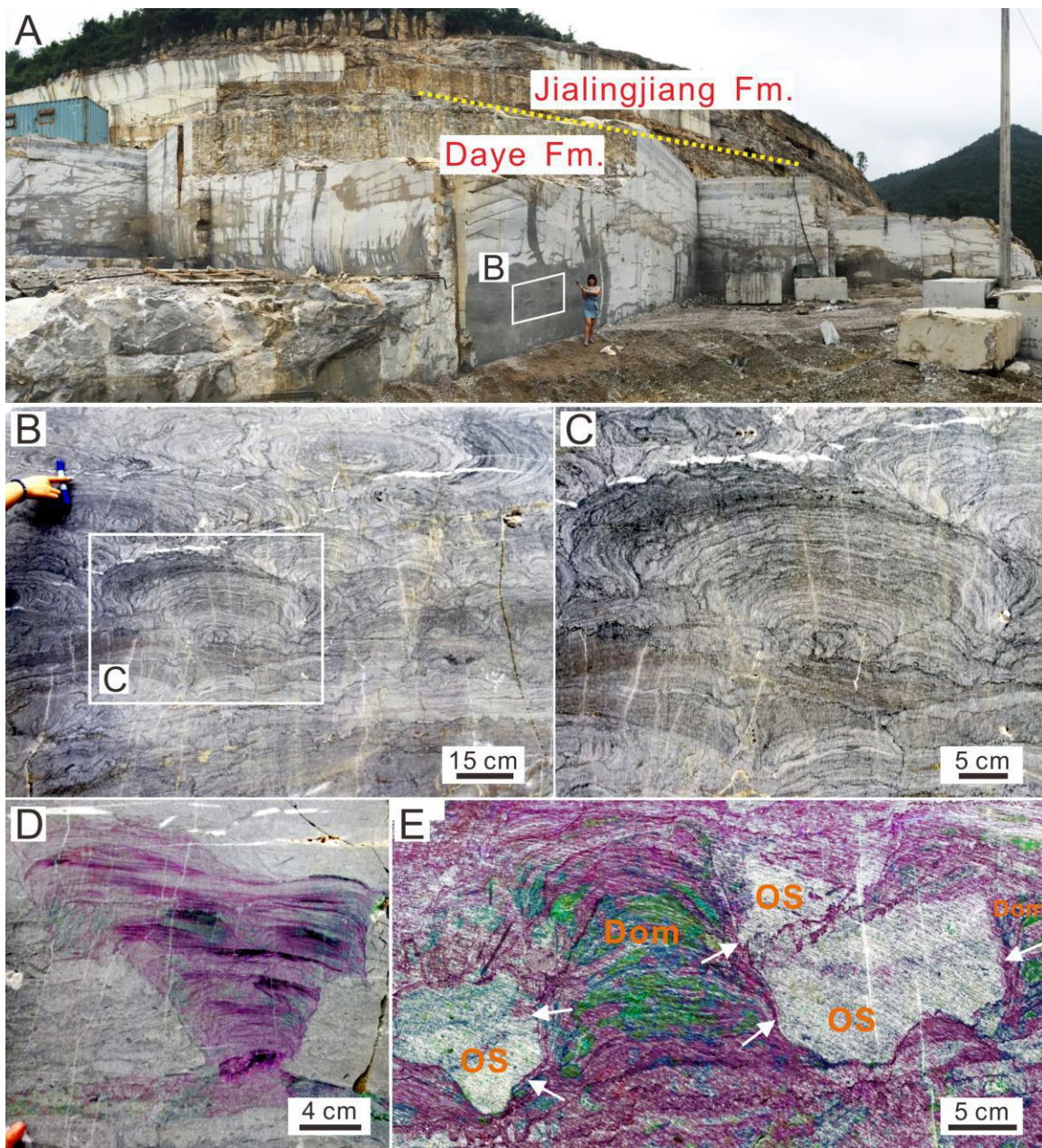
793

794

795

796

797 Figure 4



798

799

800

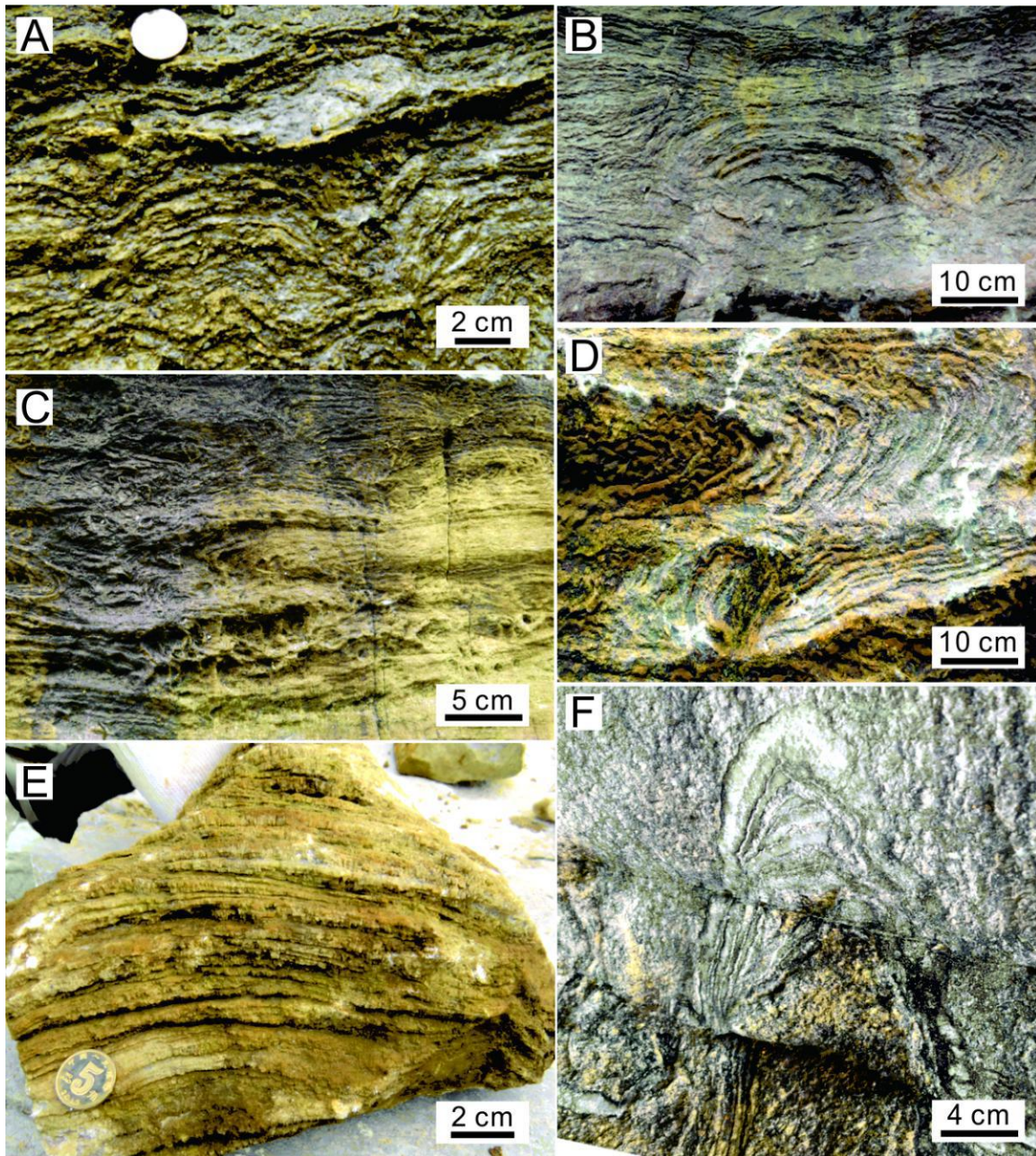
801

802

803

804

805



807

808

809

810

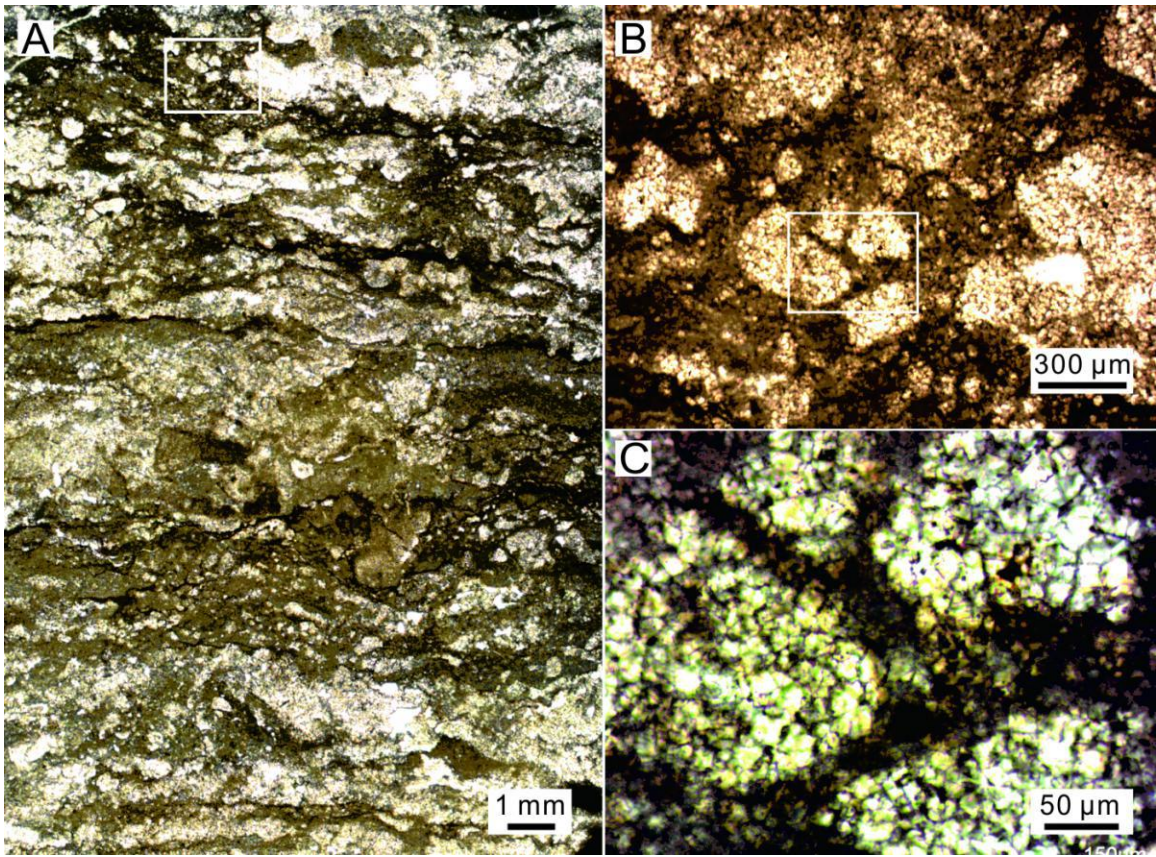
811

812

813

814

815 Figure 6



816

817

818

819

820

821

822

823

824

825

826

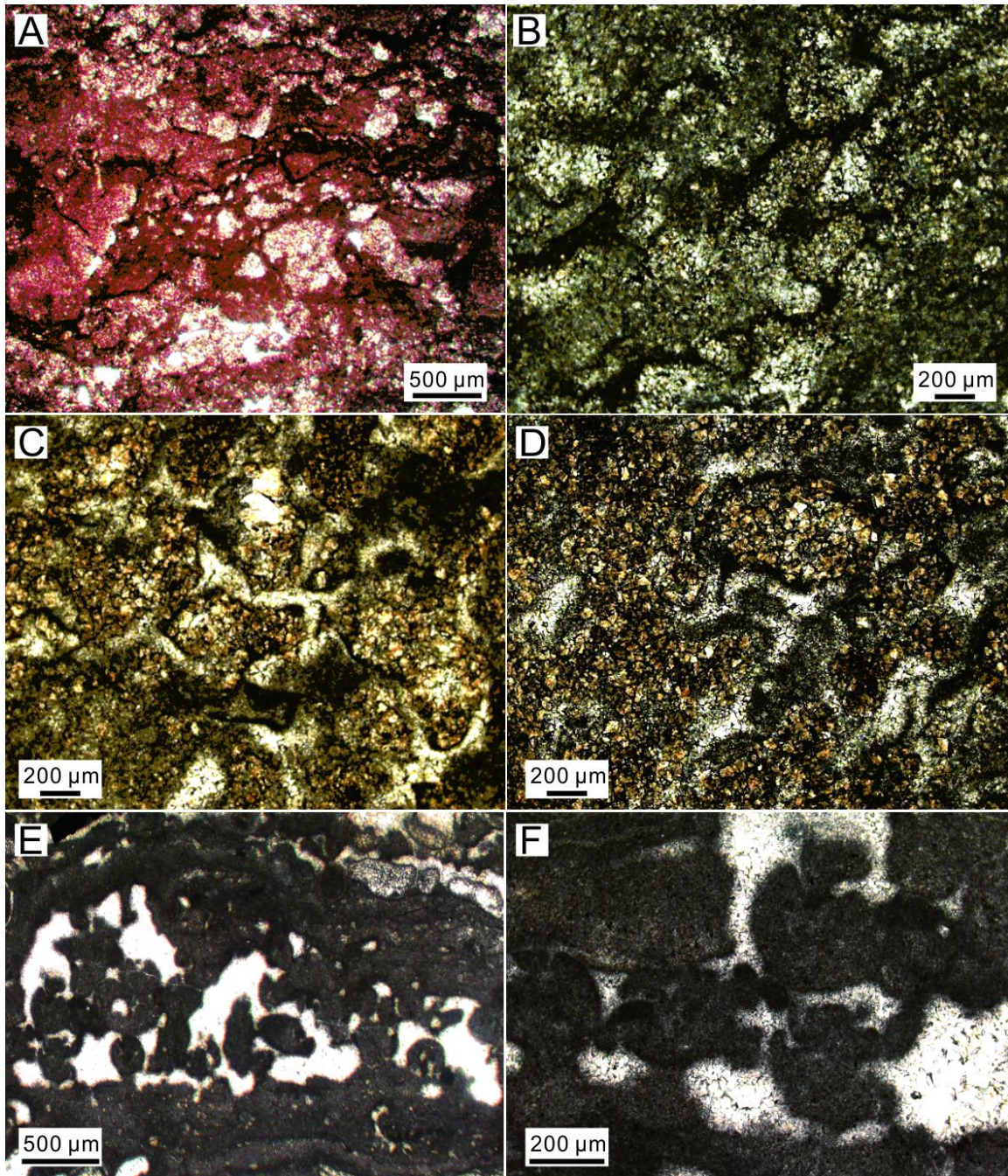
827

828

829

830

831 Figure 7



832

833

834

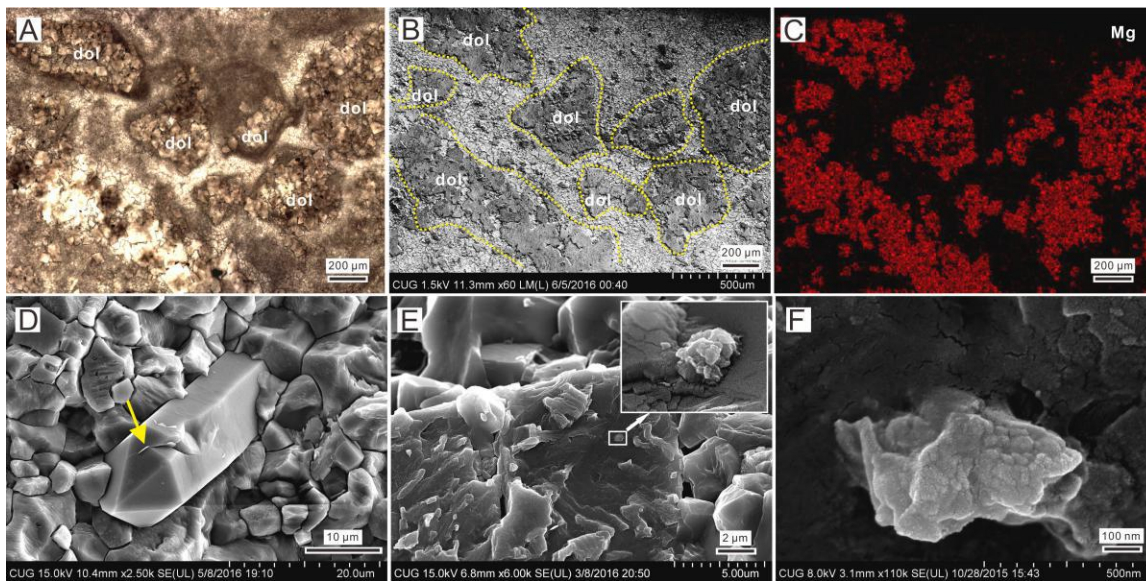
835

836

837

838

839 Figure 8



840

841

842

843

844

845

846

847

848

849

850

851

852

853

854

855

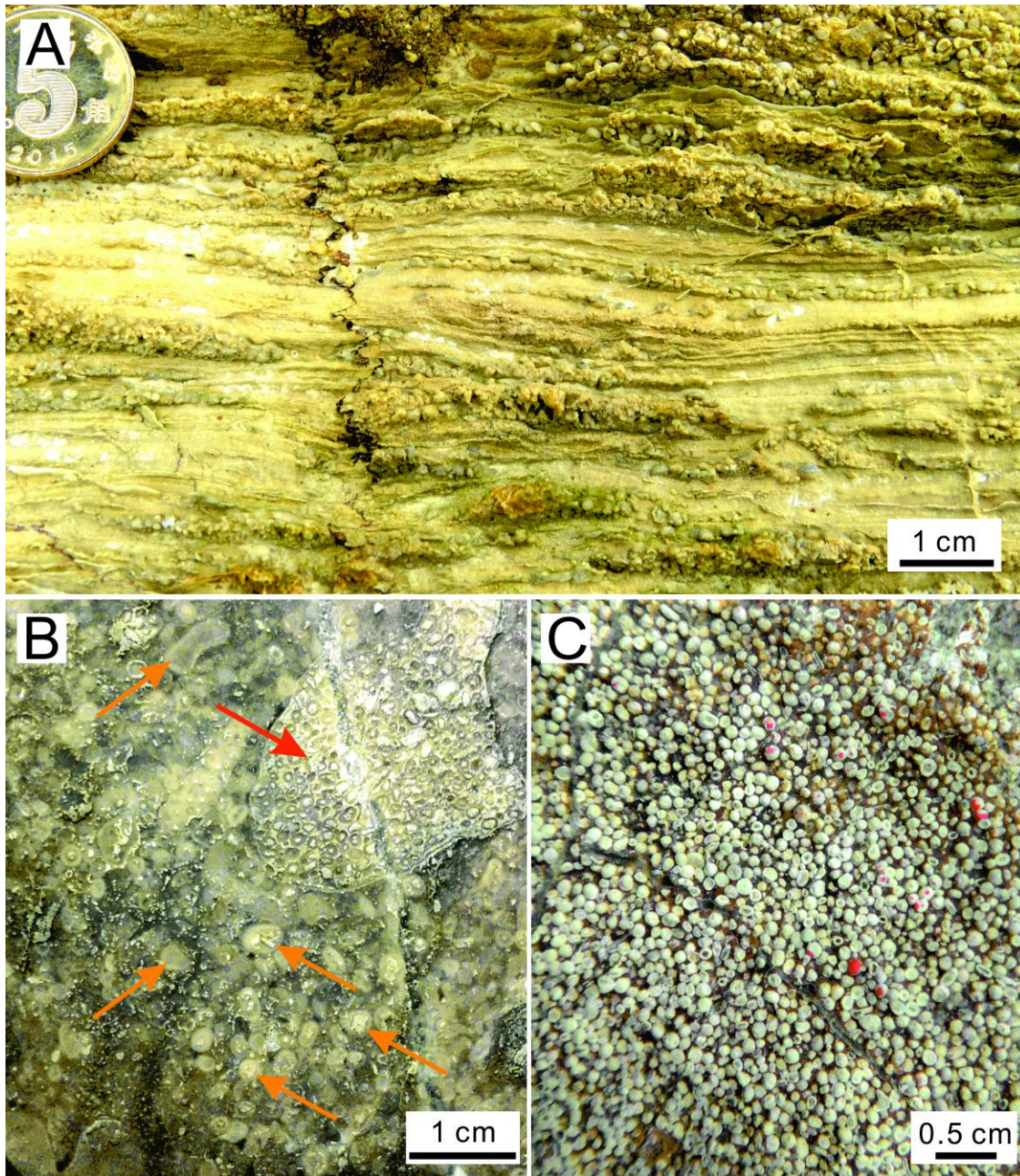
856

857

858

859

860 Figure 9



861

862

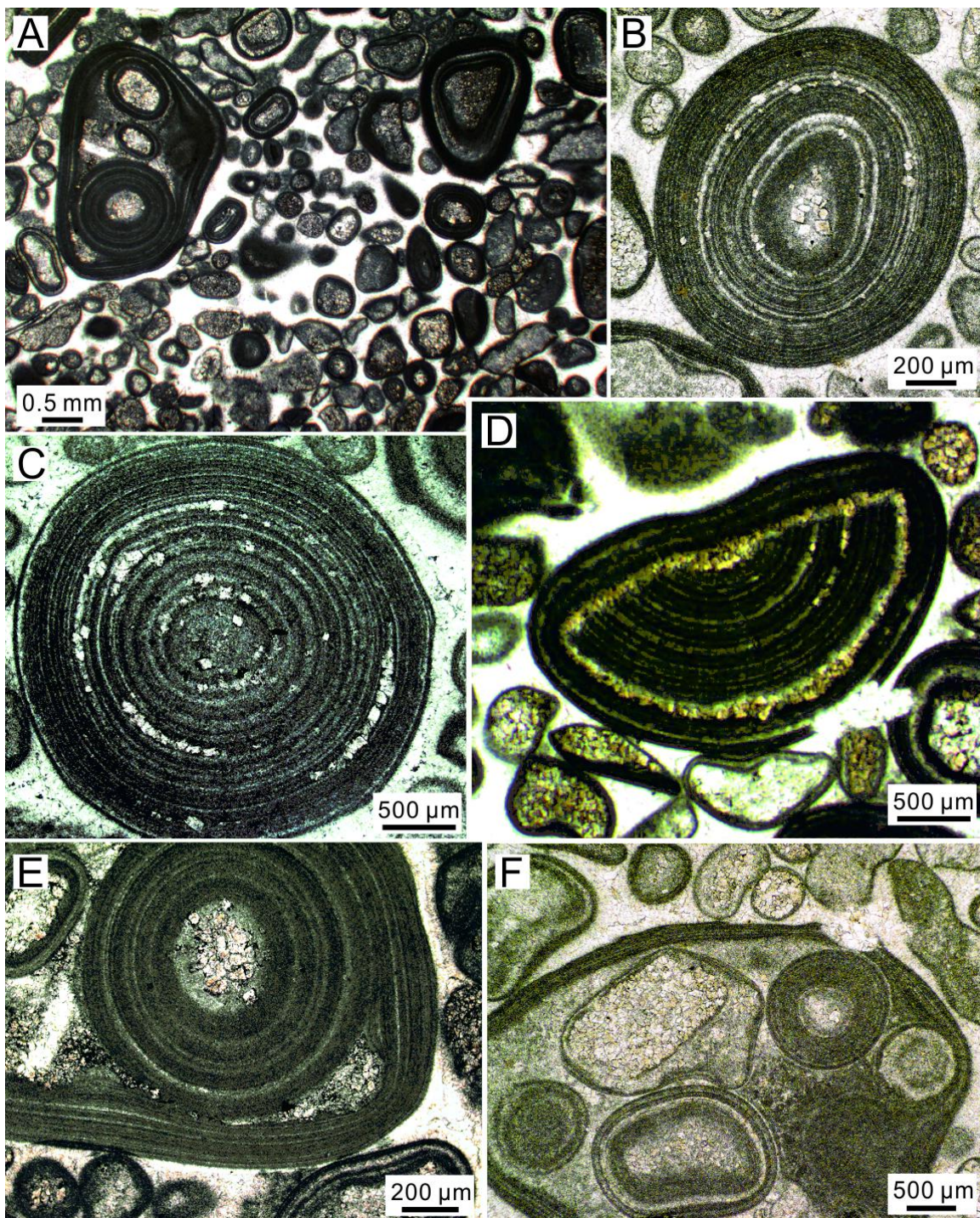
863

864

865

866

867



869

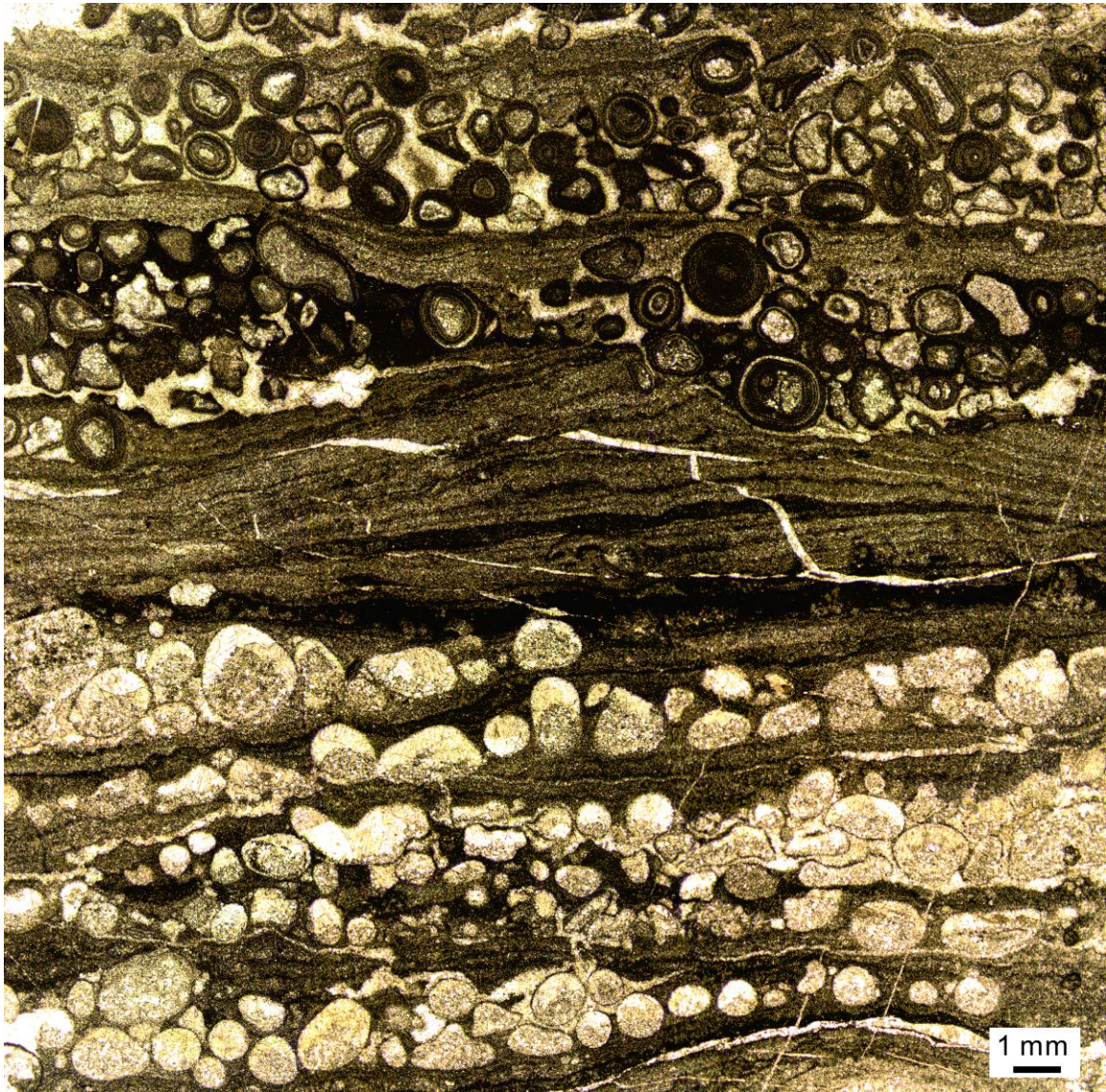
870

871

872

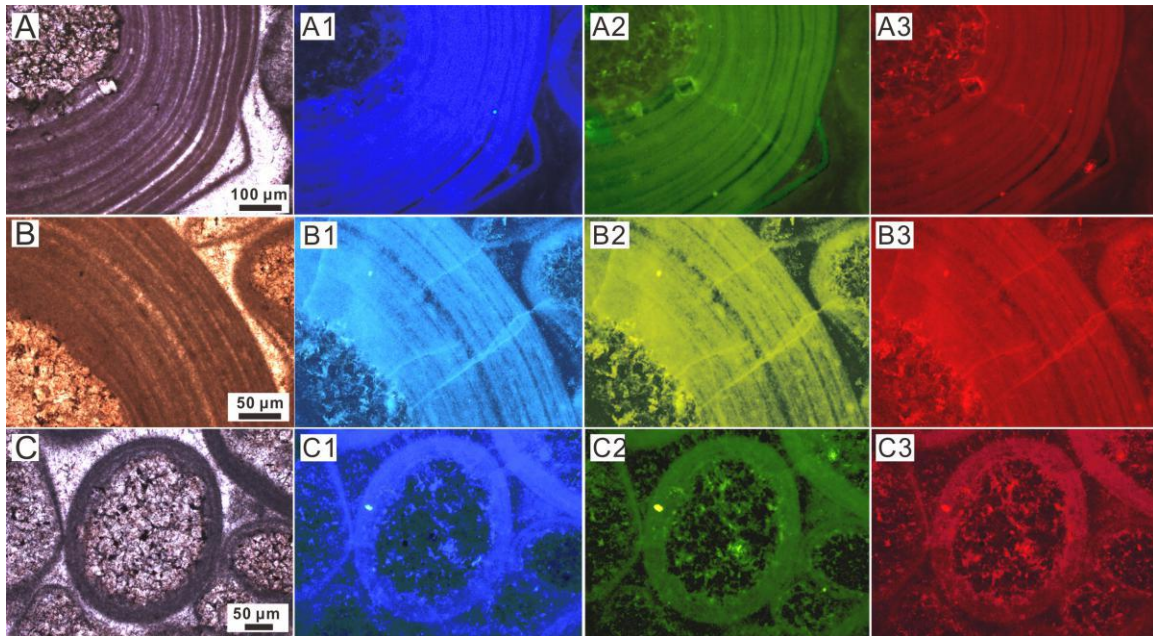
873

874 Figure 11



875
876
877
878
879
880
881
882
883
884

885 Figure 12



886

887

888

889

890

891

892

893

894

895

896

897

898

899

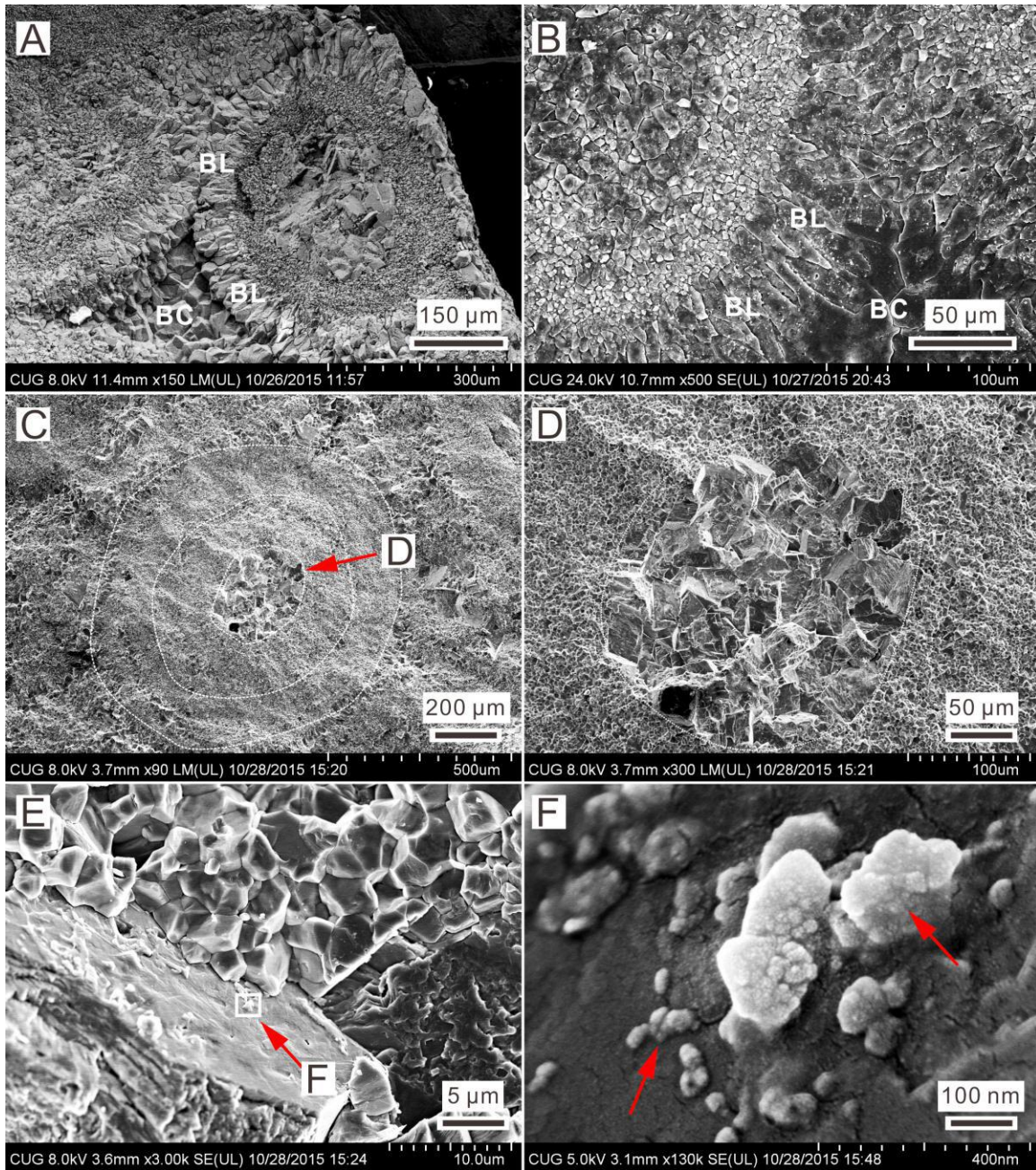
900

901

902

903

904



906

907

908

909

910

911

912

913 Figure 14

